Isotope shift factors for the Cd^+ $5s\,^2S_{1/2} \rightarrow 5p\,^2P_{3/2}$ transition and determination of Cd nuclear charge radii

J. Z. Han,[1,2] C. Pan,[3] K. Y. Zhang,[3] X. F. Yang,[3] S. Q. Zhang,[3] J. C. Berengut,[4] S. Goriely,[5] H. Wang,[6] Y. M. Yu,[7,8,*] J. Meng,[3,†] J. W. Zhang,[1,‡] and L. J. Wang[1,2,§]

[1]*State Key Laboratory of Precision Measurement Technology and Instruments, Key Laboratory of Photon Measurement and Control Technology of Ministry of Education, Department of Precision Instrument, Tsinghua University, Beijing 100084, China*

[2]*Department of Physics, Tsinghua University, Beijing 100084, China*

[3]*State Key Laboratory of Nuclear Physics and Technology, School of Physics, Peking University, Beijing 100871, China*

[4]*School of Physics, University of New South Wales, Sydney 2052, Australia*

[5]*Institut d'Astronomie et d'Astrophysique, CP-226, Universite Libré de Bruxelles, Brussels 1050, Belgium*

[6]*School of Economics and Management, Tsinghua University, Beijing 100084, China*

[7]*Beijing National Laboratory for Condensed Matter Physics, Institute of Physics, Chinese Academy of Sciences, Beijing 100190, China*

[8]*University of Chinese Academy of Sciences, Beijing 100049, China*

(Received 16 November 2021; revised 14 June 2022; accepted 17 June 2022; published 18 July 2022)

The accuracy of atomic isotope shift factors limits the extraction of nuclear charge radii from isotope shift measurements because determining these factors is experimentally and theoretically challenging. Here, the isotope shift of the Cd^+ $5s\,^2S_{1/2} \rightarrow 5p\,^2P_{3/2}$ transition is measured precisely using laser-induced fluorescence from a sympathetically cooled large Cd^+ ion crystal. A King-plot analysis is performed based on the new measurement to obtain accurate atomic field shift F and mass shift K factors that have been cross-checked by state-of-the-art configuration interaction plus many-body perturbation theory. The nuclear charge radii (R_{ch}) of $^{100-130}$Cd extracted using these F and K values demonstrate a near fivefold precision increase in the neutron-rich region. This work proves that accurate extraction of R_{ch} from isotope shifts is possible. New R_{ch} values reveal hidden discrepancies with previous density functional predictions in the neutron-rich region and pose strong challenges to advancements in nuclear models.

DOI: 10.1103/PhysRevResearch.4.033049

I. INTRODUCTION

As a fundamental property of an atomic nucleus, nuclear charge radius (R_{ch}) serves as an important probe in various nuclear phenomena, such as occurrence of magic numbers [1–3], shape staggering [4] and evolution [5,6], shape coexistence [7], proton [8] and neutron [9,10] halos, and neutron skins [11]. Moreover, the subtle evolution of R_{ch} along isotopic chains provides a stringent test and challenge for nuclear models. Therefore, highly accurate extraction of R_{ch} is paramount for experimental and theoretical nuclear physics. With the development of the laser spectroscopy technique, the differences in mean-square charge radii $\delta\langle r^2\rangle$ and R_{ch} can be precisely determined through the isotope shift (IS) measurement by using the laser spectroscopy [12,13]. However, the determination of R_{ch} requires knowledge of the values of the field shift F and mass shift K factors. The accuracy of the F and K factors has become the critical limiting reason in extracting the nuclear charge radii from the IS measurement, highlighting the importance of accurate F and K values.

The Cd nuclei have attracted much attention because of their unique attributes: (i) The Cd nuclei contains 48 protons, with only one pair of the magic proton number $Z = 50$, and the Cd isotopes have rich nuclear properties like the subshell effect that provides an excellent test case for nuclear model calculations [14,15]; (ii) the radioactive ion beam facility provides Cd isotopes with mass numbers ranging from 100 to 130 [13], which provides a considerably large amount of sample information regarding changes in nuclear properties with neutron number; and (iii) Cd/Cd^+ systems have many optical transitions that are suitable for the IS measurements, and the Cd^+ microwave clock and the sympathetic cooling technique [16,17] can further improve the accuracy of IS measurement. In the past, many groups have measured the IS of Cd, whereas their extracted $\delta\langle r^2\rangle$ are not consistent [13,15,18–21], and the accuracy of R_{ch} is relatively low when the neutron numbers are close to magic numbers 50 and 82 [13].

This work presents the latest results from a reevaluation of $^{100-130}$Cd R_{ch} and $\delta\langle r^2\rangle$ with the currently highest precision based on accurate atomic IS factors. The laser-induced fluorescence (LIF) spectroscopy from the sympathetically cooled

*ymyu@aphy.iphy.ac.cn
†mengj@pku.edu.cn
‡zhangjw@tsinghua.edu.cn
§lwan@mail.tsinghua.edu.cn

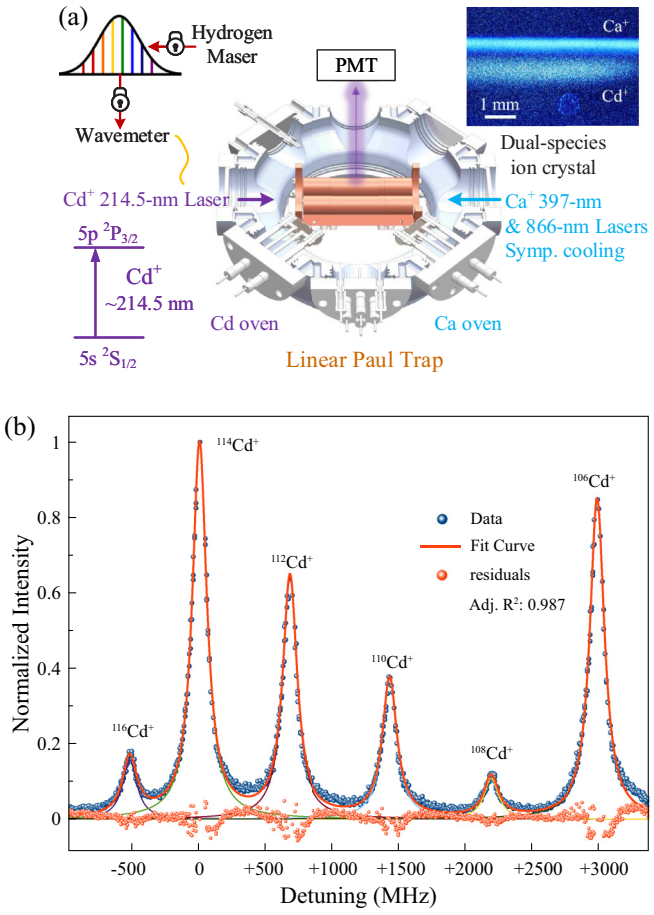

FIG. 1. (a) Experimental setup for the measurement of the IS of Cd^+ 214.5-nm transition. (b) The LIF spectrum of the Cd^+ 214.5-nm transition with the measurement points (blue dot), the fitting line (red line), the residuals (red dot) between the measurement points and the fitting line, and the adjusted $R-$squared (Adj. R^2) value of fitting.

Cd^+ ions is used to measure the IS of the $5s\,^2S_{1/2} \rightarrow 5p\,^2P_{3/2}$ (214.5-nm) transition of Cd^+ ions. A King-plot analysis is conducted to extract F and K values that are more accurate when compared with values obtained from the configuration interaction plus many-body perturbation theory (CI+MBPT). These accurate F and K values can be used to determine $\delta\langle r^2\rangle$ and $R_{\rm ch}$ of $^{100-130}$Cd with higher precision, especially for the Cd nuclei with neutron numbers approaching magic numbers $N = 50$ and 82. The more accurate Cd^+ IS factors and subsequent determination of $R_{\rm ch}$ for $^{100-130}$Cd will prompt further testing of the current nuclear theory.

II. EXPERIMENT

The IS of the Cd^+ 214.5-nm transition is measured through LIF spectroscopy using a Cd^+-Ca^+ sympathetic cooling system [17,22]. The experiment is conducted in a linear Paul trap [17] and the schematic of the setup is shown in Fig. 1(a). The Cd^+ ions are prepared from Cd atoms photoionized by a 228.8-nm (Cd $5s^2\,^1S_0 \rightarrow 5s5p\,^1P_1$) laser beam. The 423-nm (Ca $4s^2\,^1S_0 \rightarrow 4s4p\,^1P_1$) laser and 374-nm (Ca $4s4p\,^1P_1 \rightarrow$ ionized continuum) laser are used to photoionize Ca. We begin the experiment with 1 s of Doppler cooling of the Ca^+ ions that uses a 397-nm (Ca^+ $4s\,^2S_{1/2} \rightarrow 4p\,^2P_{1/2}$) laser beam and an 866-nm (Ca^+ $4p\,^2P_{1/2} \rightarrow 3d\,^2D_{3/2}$) repumping laser beam during the cooling cycle. The Coulomb interaction between Ca^+ and Cd^+ ions induces sympathetic cooling of the Cd^+ ions. A sympathetically cooled system containing approximately 4×10^5 Cd^+ ions and 2×10^5 Ca^+ ions is obtained. The temperature of Cd^+ ions is estimated to be less than 1 K using the method given in Ref. [17]. The frequency of the secular motion of the trapped ions can be calculated from [23]

$$\omega_s = \sqrt{a + \frac{q^2}{2}}\frac{\Omega}{2}, \tag{1}$$

where a and q are the parameters of the Mathieu function [23] of the linear Paul trap, and Ω represents the driving frequency of the trap. In the experiment, $a = 0$, $q = 0.065$, $\Omega = 2$ MHz, and ω_s for the Cd^+ ions is estimated to be about 0.045 MHz. The natural linewidth γ of the Cd^+ 214.5-nm transition is 60.13 MHz [22]. When $\omega_s \ll \gamma$, it is known that the Cd^+ ions are under a weakly bound condition.

The IS of the Cd^+ 214.5-nm transition is probed by scanning the laser frequency from red detuned 1000 MHz to blue detuned 3500 MHz centered on the $^{114}Cd^+$ transition frequency. The LIF spectrum is measured using a photomultiplier tube (Hamamatsu H8259-09) located at the top of the linear Paul trap [see Fig. 1(a)]. The probe laser power is maintained at less than 5 μW/mm^2 (saturation intensity 7.96 mW/mm^2 [24]), which avoids heating generated by the laser probe and through power broadening of the linewidth during the IS measurement. The resonance frequency of the 214.5-nm line is measured using a high-precision wavemeter (HighFinesse WS8-2), calibrating against an optical frequency comb referenced to a hydrogen maser.

The LIF spectrum of the Cd^+ 214.5-nm transition [Fig. 1(b)] displays six peaks that correspond to isotopes of Cd of nucleon mass numbers $A = 116$, 114, 112, 110, 108, and 106. Each data point is the average of five measurement results. The height of every peak is proportional to the natural abundance of Cd except for the low-abundance isotopes $A = 106$ and 108. The ionization laser frequency is adjusted to increase the abundance of $^{106,108}Cd^+$ in the linear Paul trap. The spectra of odd isotopes of $^{111,113}Cd^+$ are outside our measurement window and therefore do not appear in the LIF spectrum [Fig. 1(b)]. In addition, the odd isotopes such as ^{111,113}Cd have nonzero nuclear spins. The IS measurements of odd isotopes are different from those of even isotopes. The additional lasers are needed to repump the multiple transitions occurring at the hyperfine sublevels of the odd isotope. Thus, this work focuses on the isotope spectrum measurement of the even isotopes for which the hyperfine structure is absent. Under weakly bound conditions, as discussed above, the line shape of the fluorescence spectrum complies with a Voigt profile, formulated as the convolution of a Lorentz function and a Gaussian function [25–27]. Without loss of generality, we consider only centered profiles which peak at zero. The Voigt profile is then

$$V(x;\sigma,\gamma) \equiv \int_{-\infty}^{\infty} G(x';\sigma)L(x-x';\gamma)dx', \tag{2}$$

TABLE I. Isotope shift of the Cd^+ 214.5-nm transition line measured using LIF spectroscopy from the sympathetically cooled Cd^+ ions and comparisons with Ref. [13]. Numbers in parentheses are spectrum measurement uncertainties. In Ref. [13] the uncertainty due to their beam energy determination is given in brackets, which is absent in our measurement.

(A, A')	This work	Ref. [13]
(106,114)	2984.2(7)	2991.1(22)[62]
(108,114)	2188.2(19)	2194.0(22)[46]
(110,114)	1428.8(11)	1432.2(23)[30]
(112,114)	673.6(8)	674.6(22)[15]
(116,114)	−520.7(14)	−526.5(22)[15]
(108,106)	−795.9(19)	
(110,108)	−759.4(20)	
(112,110)	−755.2(11)	

where x is the shift from the line center, $G(x;\sigma)$ is the centered Gaussian profile,

$$G(x;\sigma) = \frac{e^{-x^2/(2\sigma^2)}}{\sigma\sqrt{2\pi}}, \tag{3}$$

and $L(x,\gamma)$ is the centered Lorentz profile,

$$L(x;\gamma) = \frac{\gamma}{\pi(x^2+\gamma^2)}, \tag{4}$$

where σ denotes the Gaussian linewidth, and γ is the Lorentzian linewidth, which equals the natural linewidth 60.13 MHz and is fixed during fitting. The multiple-peaks Voigt function is used to fit the LIF spectrum and determines both the center position and corresponding σ value for each peak. The σ value corresponds to the Gaussian linewidth, which has an average of 83 MHz for all the peaks. The Gaussian linewidth arises from the thermal motion of approximately 10^5 Cd^+ ions in the linear Paul trap. The spectra of the ions exhibit considerable Doppler broadening even under laser cooling due to the Coulomb repulsion of ions and radio-frequency heating of the trap. The fitted curve displays an excellent overlap with the data samples, the adjusted R-squared value of the fit being 0.987. The residuals of the measured and fitted values are low, as denoted by red circles at the bottom of Fig. 1(b). The fit uncertainty for the center peak of the $^A Cd^+$ 214-nm transition line is 0.4, 1.8, 0.9, 0.5, 0.3, and 1.2 MHz for $A = 106$, 108, 110, 112, 114, and 116, respectively.

The IS of the isotope pair (A, A') is determined by the position of each peak, as summarized in Table I. The dominant systematic uncertainties in the frequency of the IS caused by the Zeeman and Stark shifts are common for all isotopes that can be canceled out for the IS of the (A, A') pair. The Doppler shift depends on the mass of the different isotopes. However, the differential IS value resulting from the mass difference is about kilohertz, which is far less than the megahertz accuracy of our experiment. The possible instrumental uncertainty stems mainly from drifts in the wavemeter, which we estimate to be less than 0.5 MHz. The total measurement uncertainty of the IS for the (A, A') pair is determined by the square root of the sum of the squares of the fit uncertainties of the center peak positions of A and A' and the instrumental uncertainty, which are given in the parentheses in Table I. This accuracy is better than the previous best results [13]. The sympathetic cooling technique enhances the signal-to-noise ratio and is advantageous in trapping different isotopes, including the low-abundance isotopes 106 and 108.

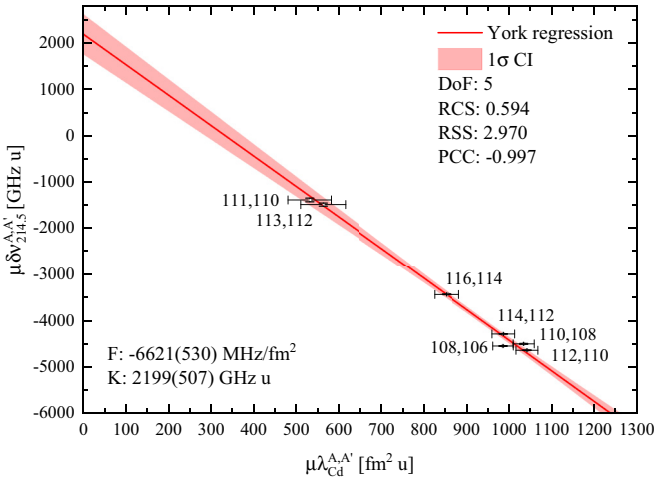

FIG. 2. King-plot analysis of the modified IS $\mu\delta\nu_{214.5}$ of the Cd^+ 214.5-nm transition and the modified nuclear size parameter $\mu\lambda_{Cd}$. The red regression line is obtained by the York regression [30] of the least-squares estimation considering the uncertainties of both $\mu\delta\nu_{214.5}$ and $\mu\lambda_{Cd}$. The red shadow region denotes the 1σ confidence intervals (CI) of the regression line. The degree of freedom (DoF), reduced chi-square (RCS), residual sum of squares (RSS), and Pearson correlation coefficient (PCC) of the fit line are given.

III. KING-PLOT ANALYSIS

The energy shift $\delta\nu^{A,A'}$ of a transition frequency ν in an isotope A with respect to another isotope A' is expressed as

$$\mu\delta\nu^{A,A'} = F\mu\lambda^{A,A'} + K, \tag{5}$$

where $\mu = m^A m^{A'}/(m^A - m^{A'})$ is calculated based on the nuclear mass in Ref. [28], and λ is the nuclear size parameter obtained by muonic atom spectroscopy and electron scattering experiments. Based on Eq. (5), the values of F and K can be estimated by the King-plot analysis [29] that is constructed by using $\mu\lambda^{A,A'}$ and $\mu\delta\nu^{A,A'}$ to be the X and Y variables. The intercept a and the slope b of the best fitting straight line of $\mu\delta\nu^{A,A'}$ versus $\mu\lambda^{A,A'}$ are F and K, respectively.

We perform a King-plot analysis (Fig. 2) based on seven isotope pairs of $(A, A') = (108, 106)$, (110,108), (112,110), (114,112), (116,114), (111,110), and (113,112). The $\mu\delta\nu^{A,A'}_{214.5}$ values for (108,106), (110,108), (112,110), (114,112), and (116,114) are obtained adopting our measurement results given in Table I, whereas those for (111,110) and (113,112) are taken from Ref. [13]. Isotope pairs in Ref. [13] that have no λ values available are not included in the King-plot analysis (input data are given in Table IV of Appendix 1). Here, "York regression" [30] is used to evaluate a and b and their errors σ_a^2 and σ_b^2. The regression algorithm considers the correlation between the uncertainties of the X and Y variables based on the least-squares method. The parameters a, b, σ_a^2, and σ_b^2 for

the regression are expressed as [30]

$$F \equiv b = \frac{\sum W_i \beta_i V_i}{\sum W_i \beta_i U_i} \tag{6}$$

and

$$K \equiv a = \overline{\mu\delta\nu} - F\overline{\mu\lambda}, \tag{7}$$

where

$$W_i = \frac{\omega(\mu\lambda_i)\omega(\mu\delta\nu_i)}{\omega(\mu\lambda_i) + b^2\omega(\mu\delta\nu_i) - 2br_i\alpha_i}, \tag{8}$$

$$\beta_i = W_i\left[\frac{U_i}{\omega(\mu\lambda_i)} + \frac{bV_i}{\omega(\mu\delta\nu_i)} - (bU_i + V_i)\frac{r_i}{\alpha_i}\right], \tag{9}$$

and the weights $\omega(\mu\lambda_i)$ and $\omega(\mu\delta\nu_i)$ for each data point are determined by $\omega(\mu\lambda_i) = 1/\sigma^2(\mu\lambda_i)$ and $1/\omega(\mu\delta\nu_i) = \sigma^2(\mu\delta\nu_i)$, where $\sigma(\mu\lambda_i)$ and $\sigma(\mu\delta\nu_i)$ are the uncertainties of $\mu\delta\nu_i$ and $\mu\lambda_i$, and $\alpha_i = \sqrt{\omega(\mu\lambda_i)\omega(\mu\delta\nu_i)}$ is the weight parameter, and

$$r_i = \frac{\sum[\sigma(\mu\lambda_i) - \overline{\sigma(\mu\lambda)}][\sigma(\mu\delta\nu_i) - \overline{\sigma(\mu\delta\nu)}]}{\sqrt{\sum[\sigma(\mu\lambda_i) - \overline{\sigma(\mu\lambda)}]^2 \sum[\sigma(\mu\delta\nu_i) - \overline{\sigma(\mu\delta\nu)}]^2}} \tag{10}$$

is the correlation coefficient between $\sigma(\mu\lambda_i)$ and $\sigma(\mu\delta\nu_i)$. The mean values $\overline{\mu\delta\nu}$ and $\overline{\mu\lambda}$ are

$$\overline{\mu\delta\nu} = \frac{\sum W_i \mu\delta\nu_i}{\sum W_i}, \tag{11}$$

$$\overline{\mu\delta\lambda} = \frac{\sum W_i \mu\delta\lambda_i}{\sum W_i} \tag{12}$$

and

$$V_i = \mu\delta\nu_i - \overline{\mu\delta\nu}, \tag{13}$$

$$U_i = \mu\lambda_i - \overline{\mu\lambda}. \tag{14}$$

By iterating, we can calculate the F and K parameters and their corresponding uncertainties $\sigma(F)$ and $\sigma(K)$. The $\sigma(F)$ and $\sigma(K)$ are written as

$$\sigma^2(F) \equiv \sigma_b^2 = \frac{1}{\sum W_i u_i^2}. \tag{15}$$

$$\sigma^2(K) \equiv \sigma_b^2 = \frac{1}{\sum W_i} + \bar{x}^2\frac{1}{\sum W_i u_i^2}, \tag{16}$$

where $u_i = x_i - \bar{x}$ is defined on the regression-adjusted points (x_i, y_i) falling on the regression best straight line and the mean value $\bar{x} = \sum W_i x_i$. The regression yields $F = -6621(530)$ MHz/fm^2 and $K = 2199(507)$ GHz u for the Cd^+ 214.5-nm transition, which is consistent with the previous results [13] but has a much lower uncertainty. Note that the (108,106) data point lies outside the regression line which may have arisen because of missing electron scattering data.

IV. ATOMIC STRUCTURE CALCULATION

The atomic structure calculation starts from a self-consistent Dirac-Fock-Breit (DFB) calculation in the potential of a closed-shell Pd-like core. The one-electron Dirac-Fock (DF) operator in atomic units $\hbar = e = m_e = 1$ ($\hbar$ is Plank constant, e is electron charge, and m_e is electron mass) is

$$h_{\rm DF} = c\,\boldsymbol{\alpha}\cdot\mathbf{p} + (\beta - 1)c^2 - \frac{Z}{r} + V^{N_{\rm DF}}, \tag{17}$$

where $\boldsymbol{\alpha}$ and β are the Dirac matrices, c is the light speed, Z is the atomic number, and r is the position of electron. $V^{\rm DF}$ includes the direct and exchange parts of the Dirac-Fock interaction with the Pd-like core. The DF operator at this stage is modified to include the Breit interaction

$$B_{i,j} = -\frac{1}{2r_{ij}}\left[\boldsymbol{\alpha}_i\cdot\boldsymbol{\alpha}_j + (\boldsymbol{\alpha}_i\cdot\mathbf{r}_{ij})(\boldsymbol{\alpha}_i\cdot\mathbf{r}_{ij})/\mathbf{r}_{ij}^2\right]. \tag{18}$$

Next, a large valence basis of one-particle orbitals is generated by diagonalizing a set of B splines over the one-electron DFB operator. Many-electron configurations for the CI expansion are constructed with these orbitals. For Cd^+, we need to access the hole states, so we employ a particle-hole CI+MBPT [33], for which the core $4d$ shell is unfrozen and included in the CI configurations. The configuration set is generated from all single and double excitations up to $10spdf$ from leading configurations $5s$, $5p$, $5d$, and $4d^{-1}5s^2$. Correlations with core shells not included in the CI expansion use the MBPT for both Cd and Cd^+. This includes excitations to virtual orbitals up to $30spdfg$. For neutral Cd, the CI configurations include all valence excitations from the leading configuration $5s^2$ and $5s5p$ up to level $20spdf$, but hole correlations are less important and are only included in MBPT. In addition to the Cd^+ 214.5-nm transition, we also calculate the IS factors of three important transitions in Cd/Cd^+ that are Cd^+ $5s\,^2S_{1/2}$-$5p\,^2P_{1/2}$ (226.5 nm), Cd $5s5p\,^3P_2$-$5s6s\,^3S_1$ (508.6 nm), and Cd $5s^2\,^1S_0$-$5s5p\,^3P_1$ (326.1 nm) transitions. The CI+MBPT calculation reproduces the transition energies of the Cd^+ 214.5-nm and 226.5-nm transitions and the Cd 508.6-nm and 326.1-nm transitions within a 2% accuracy for the calculation of the F and K factors, such accuracy is sufficient.

The normal mass shift and the field shift are calculated by modifying the Dirac-Fock operator. The normal mass shift constant can be expressed in atomic units as

$$k_{\rm NMS} = \frac{1}{2m_u}\sum_i p_i^2, \tag{19}$$

where $m_u = 1823$ is the ratio of the atomic mass unit to the electron mass and the sum is over all electron momenta $\mathbf{p}_i$. A scaling factor λ ahead of the $k_{\rm NMS}$ operator is added in the finite field scaling calculation. The specific mass shift constant is

$$k_{\rm SMS} = \frac{1}{m_u}\sum_{i<j}\mathbf{p}_i\cdot\mathbf{p}_j, \tag{20}$$

and in order to calculate $k_{\rm SMS}$ in the finite-field scaling method, a rescaled two-body SMS operator is added to the Coulomb potential everywhere that it appears in an energy calculation,

$$\tilde{Q} = \frac{1}{\mathbf{r}_1 - \mathbf{r}_2} + \lambda\mathbf{p}_1\cdot\mathbf{p}_2. \tag{21}$$

Note that we use a relativistic formulation of the mass shift that reduces to the equations above in the nonrelativistic limit.

TABLE II. F and K factors for Cd^+ and Cd obtained from the King-plot analysis and the CI+MBPT calculations and comparisons with the early King-plot and semiempirical theoretical results.

F (MHz/fm^2)	K (GHz u)	Sources
Cd^+ $5s\,^2S_{1/2}$-$5p\,^2P_{3/2}$ (214.5 nm)		
−6621(530)	2199(507)	King plot
−6144(300)	1667(300)	CI+MBPT
−6260(1860)	1860(1920)	King plot [13]
Cd $5s5p\,^3P_2$-$5s6s\,^3S_1$ (508.6 nm)		
1300(110)	−112(105)	King plot[a]
1228(60)	−63(400)	CI+MBPT
Cd^+ $5s\,^2S_{1/2}$-$5p\,^2P_{1/2}$ (226.5 nm)		
−6067(300)	1770(300)	CI+MBPT
−6077(734)	1468(734)	Semiempirical [31]
−6174(778)	558(385)	Semiempirical [32]
Cd $5s^2\,^1S_0$-$5s5p\,^3P_1$ (326.1 nm)		
−4559(230)	1865(400)	CI+MBPT
−4420(340)	1717(330)	King plot [18]
−3910(460)	876(230)	Semiempirical [21]
−3900(460)	809(407)	Semiempirical [20]

[a]King plot is made by using the IS data of Ref. [13].

We perform multiple almost identical CI+MBPT calculations which differ only in λ, and the $K_{\rm NMS}$ or $K_{\rm SMS}$ are extracted by

$$K_{\rm NMS,SMS} = \left.\frac{d\nu}{d\lambda}\right|_{\lambda=0}. \tag{22}$$

The field shift component of the IS is given by

$$\delta\nu^{A',A} = F\delta\langle r^2\rangle^{A',A} = F\left(\langle r^2_{A'}\rangle - \langle r^2_A\rangle\right), \tag{23}$$

where $\langle r^2\rangle$ is the mean-square charge radius. The field shift constant, F, is extracted by varying the nuclear radius in the code (in AMBIT the nuclear charge has a Fermi distribution) and taking the derivative

$$F = \frac{d\nu}{d\langle r^2\rangle}, \tag{24}$$

at the physical point.

Table II summarizes the values of the F and K factors. For the Cd^+ 214.5-nm transition, the CI+MBPT results for F are consistent with our King-plot results and Ref. [13] within an 8% deviation. The CI+MBPT results for K are lower than the King-plot data by 30%, where the 30% difference is well within the combined uncertainty. For the isotopes of $A = 117, 118, 119, 120, 122$, the IS measurement of the Cd $5s5p\,^3P_2 \rightarrow 5s6s\,^3S_1$ (508.6-nm) transition has relatively high accuracy [13]. A King-plot analysis adopting the IS values of Ref. [13] is performed to extract the $R_{\rm ch}$ in $^{117\text{–}120,122}$Cd, and the results are compared with the CI+MBPT results; an agreement within the uncertainties is obtained. For the Cd^+ 226.5-nm transition, the F factor calculated by the CI+MBPT is in excellent agreement with early semiempirical data, whereas the K factor calculated by the CI+MBPT seems to support the result of Bishop and King [31] and differs from the result of Bauche *et al.* [32]. For the Cd 326.1-nm transition, the F and K factors calculated by the CI+MBPT are consistent with the King-plot results [18], indicating that the early semiempirical work [20,21] may have underestimated the F and K values.

Accurate calculations of F and K factors are a substantial challenge for many-body atomic theory. Although the CI+MBPT method was checked for accuracy and reliability in calculations of the atomic factors of other monovalent ions and neutral atom systems (see, e.g., Ca^+ [12,34,35] and Yb^+ [36]), for the specific mass shift, with the CI+MBPT method it is hard to achieve a result better than 20%–30% accuracy [37], and the CI+MBPT calculation also showed a difference with another theoretical method [38]. In this work, the uncertainties in F and K are estimated according to the influence of the more extensive configuration expansion and higher-order correlations, and they are given in parentheses in Table II.

V. NUCLEAR CHARGE RADII OF $^{100\text{–}130}$Cd

On the basis of the above King-plot analysis, $\delta\langle r^2\rangle$ and $R_{\rm ch}$ of $^{100\text{–}130}$Cd can be extracted with higher accuracy. The values for F and K are obtained based on seven isotope pairs that have available measured values of λ. Then the values of λ for all isotopes can be determined in terms of Eq. (5) for given measured values of $\delta\nu^{A,A'}$. An individual linear transformation $\mu\lambda_{\rm Cd} \rightarrow (\mu\lambda_{\rm Cd} - \alpha)$ [13,35] is used to simplify the correlation between F and K, where α denotes a parameter of the linear transformation. We then perform a linear transformation for individual isotopes to obtain F and K_α. Finally, the $\delta\langle r^2\rangle$ value is determined using

$$\begin{aligned}\lambda^{A,A'} &= \frac{\delta\nu^{A,A'} - K_\alpha/\mu^{A,A'}}{F} + \frac{\alpha}{\mu^{A,A'}} \\ &= \delta\langle r^2\rangle^{A,A'} + \frac{C_2}{C_1}\delta\langle r^4\rangle^{A,A'} + \frac{C_3}{C_1}\delta\langle r^6\rangle^{A,A'} \\ &\approx 0.973\,\delta\langle r^2\rangle^{A,A'},\end{aligned} \tag{25}$$

where $C_{1,2,3}$ denote the coefficients associated with contributions from higher radial moments [39]. The higher-order terms have −2.7% contribution to the determination of the $\delta\langle r^2\rangle$ [18], therefore we choose a parameter 0.973 to take into account the role of the higher-order terms [13].

The values of $\delta\langle r^2\rangle^{A,114}$ and $R_{\rm ch}$ for $^{100\text{–}130}$Cd are summarized in Table III. The difference in $\delta\langle r^2\rangle^{A,114}$ between this work and Ref. [13] increases from 0 to 0.012 when A changes from 114 to 100 and from 0 to 0.008 when A changes from 114 to 130. The uncertainties in $\delta\langle r^2\rangle^{A,114}$ have three sources that arise from $\delta\nu^{A,114}$, F, and K_α. Specifically, the uncertainty in $\delta\langle r^2\rangle^{A,114}$ arising from F and K_α is estimated to be $\sqrt{\sigma(\delta\langle r^2\rangle^{A,114})|_F^2 + \sigma(\delta\langle r^2\rangle^{A,114})|_{K_\alpha}^2}$, for which

$$\begin{aligned}\sigma(\delta\langle r^2\rangle^{A,114})|_F &= \left|\frac{-(\delta\nu^{A,114} - K_\alpha/\mu^{A,114})\sigma(F)}{0.973F^2}\right|, \\ \sigma(\delta\langle r^2\rangle^{A,114})|_{K_\alpha} &= \left|\frac{-\sigma(K_\alpha)}{0.973F\mu^{A,114}}\right|.\end{aligned} \tag{26}$$

The extracted $R_{\rm ch}$ of this work and Ref. [13] are compared in Fig. 3. The more accurate F and K factors yield a precise determination of $R_{\rm ch}$, especially for isotopes from the

TABLE III. The $\delta\langle r^2\rangle^{A,114}$ (fm^2) and R_{ch} (fm) values of $^{100-130}$Cd extracted from $\delta\nu^{A,114}$, as taken from our Cd^+ 214.5-nm line measurement results (*), the Cd 508.6-nm line (†), and the Cd^+ 214.5-nm line (untagged) measurement results in Ref. [13]. The linear transformation parameters, α (fm^2 u) and K_α (GHz u), are individually for each isotope. For $\delta\langle r^2\rangle^{A,114}$ and R_{ch}, uncertainties caused by the errors in $\delta\nu^{A,114}$, and the errors in F and K_α are given in the first and second parentheses. The measurement uncertainty of R_{ch} in ^{114}Cd is given in the third parentheses. The column under "Difference" compares $\delta\langle r^2\rangle^{A,114}$ of this work and Ref. [13]. For explanations for the numbers in parenthese and brackets in $\delta\nu^{A,114}$ see the caption of Table I.

A	$\delta\nu^{A,114}$	α	K_α	$\delta\langle r^2\rangle^{A,114}$	$\delta\langle r^2\rangle^{A,114}$ [13]	Difference	R_{ch}
100	6371.6(31)[114]	1030	−4621(85)	−1.409(5)(18)	−1.421(5)(43)	0.012	4.4567(6)(21)(10)
101	5859.9(22)[105]	1031	−4627(86)	−1.295(4)(17)	−1.307(4)(40)	0.012	4.4694(4)(19)(10)
102	5037.2(24)[87]	1007	−4468(80)	−1.135(3)(14)	−1.144(3)(25)	0.009	4.4873(3)(15)(10)
103	4621.6(24)[79]	1011	−4495(81)	−1.038(3)(13)	−1.046(3)(24)	0.008	4.4981(3)(14)(10)
104	3922.7(24)[79]	990	−4356(77)	−0.897(2)(10)	−0.904(2)(16)	0.007	4.5137(2)(12)(10)
105	3608.7(22)[70]	1001	−4429(78)	−0.817(2)(10)	−0.823(2)(16)	0.006	4.5225(2)(11)(10)
106	2984.2(7)*	979	−4283(75)	−0.690(1)(8)	−0.695(2)(12)	0.005	4.5366(1)(9)(10)
107	2730.9(23)[54]	998	−4409(78)	−0.620(2)(7)	−0.625(2)(12)	0.005	4.5443(2)(8)(10)
108	2188.2(19)*	977	−4270(75)	−0.506(1)(6)	−0.510(1)(9)	0.004	4.5568(1)(6)(10)
109	1958.3(22)[38]	1006	−4462(80)	−0.442(1)(5)	−0.445(1)(9)	0.003	4.5639(1)(6)(10)
110	1428.8(11)*	976	−4263(75)	−0.331(1)(4)	−0.334(1)(6)	0.003	4.5760(1)(4)(10)
111	1314.3(22)[23]	1057	−4799(94)	−0.285(1)(4)	−0.288(1)(12)	0.003	4.5810(1)(4)(10)
112	673.6(8)*	963	−4177(73)	−0.158(1)(2)	−0.159(1)(4)	0.001	4.5948(1)(2)(10)
113	555.2(23)[8]	1178	−5601(143)	−0.113(1)(2)	−0.114(1)(10)	0.001	4.5998(1)(2)(10)
114	0			0	0	0	4.6120(0)(0)(10)
115	−110.4(29)[7]	748	−2753(128)	0.043(1)(2)	0.043(1)(12)	0.000	4.6167(1)(2)(10)
116	−520.7(14)*	898	−3747(77)	0.134(1)(2)	0.134(1)(8)	0.000	4.6264(1)(2)(10)
117	192.9(11)[21]†	841	982(19)	0.172(1)(4)	0.171(1)(8)	0.001	4.6306(1)(4)(10)
118	275.5(20)[14]†	867	1016(17)	0.244(3)(5)	0.243(3)(22)	0.001	4.6384(3)(5)(10)
119	319.0(10)[32]†	844	986(19)	0.285(3)(6)	0.283(3)(33)	0.002	4.6428(3)(7)(10)
120	386.5(10)[21]†	850	994(18)	0.344(3)(7)	0.342(3)(37)	0.002	4.6492(3)(8)(10)
121	−1309.3(40)[50]	833	−3316(94)	0.377(4)(9)	0.375(4)(49)	0.002	4.6527(4)(9)(10)
122	484.9(11)[27]†	835	974(19)	0.434(5)(10)	0.431(5)(54)	0.003	4.6588(5)(11)(10)
123	−1551.5(37)[65]	821	−3237(98)	0.461(6)(12)	0.457(6)(67)	0.004	4.6617(6)(13)(10)
124	−1748.2(22)[72]	825	−3263(97)	0.514(6)(13)	0.510(6)(72)	0.004	4.6674(6)(14)(10)
125	−1757.3(35)[79]	810	−3164(102)	0.537(7)(15)	0.533(7)(86)	0.004	4.6699(7)(16)(10)
126	−1957.6(22)[86]	815	−3197(101)	0.590(8)(16)	0.585(8)(90)	0.005	4.6755(9)(17)(10)
127	−1912.3(30)[94]	799	−3091(107)	0.604(9)(18)	0.599(9)(106)	0.005	4.6771(10)(20)(10)
128	−2171.6(23)[100]	809	−3157(103)	0.666(9)(19)	0.660(9)(107)	0.006	4.6836(10)(20)(10)
129	−1911.1(55)[108]	780	−2965(114)	0.646(12)(23)	0.638(12)(133)	0.008	4.6815(13)(24)(10)
130	−2208.1(33)[115]	793	−3051(109)	0.713(11)(23)	0.705(11)(132)	0.008	4.6886(12)(24)(10)

neutron-deficient ($N < 60$) and neutron-rich ($N > 70$) regions. The linear transform for the individual isotope has K_α and $\sigma(K_\alpha)$ values specific to each isotope, which should be advantageous for the decrease of the uncertainties of $\delta\langle r^2\rangle^{A,114}$ caused by uncertainties of the F and K factors. Our R_{ch} values agree with Ref. [13], lying well within their uncertainties but with much-improved accuracy. For the neutron-rich region, the R_{ch} accuracy has been improved nearly five times. The improved accuracy highlights the odd-even staggering (OES) of R_{ch} in Cd isotopes for $N > 70$, the phase of which is uncertain in previous works.

The present high-precision results of R_{ch} in $^{100-130}$Cd set a formidable benchmark for the latest advances in nuclear theory. In Fig. 3, we include two modern theoretical predictions for comparison: Fayans functional Fy(Δr) [13,40] and one of the best fits of Skyrme-Hartree-Fock-Bogoliubov mass formula, HFB-24 [41] (values are given in Table V of Appendix 2). Note that other predictions from different density functional calculations have been compared in Ref. [13], but most fail to reproduce the isotopic trend as a whole and OES in detail. The Fy(Δr) model, which includes gradient terms in surface term and pairing functional [40,42], reproduces satisfyingly the experimental data. This functional is tuned with the Ca chain [40] and performs well for the Cd chain, capturing not only the isotopic trend but also the correct phase of OES.

Nevertheless, the Fy(Δr) results for neutron-rich Cd nuclei near $N = 82$, which are within the errors of previous experimental data, are now beyond the high-accuracy results obtained in this work. The amplitudes of OES are generally overestimated by Fy(Δr), similar to its description for potassium isotopes [1]. The HFB-24, in which the strength in contact pairing for neutrons (protons) depends on the neutron and proton densities, provides a remarkable quantitative description of the experimental data. However, some apparent discrepancies exist in the OES, e.g., the opposite phase near $N = 80$. Other best Skyrme HFB mass formulas [41,43,44] show similar performances as HFB-24. Therefore, the present $^{100-130}$Cd R_{ch}, with improved accuracy, particularly for the neutron-rich region, is set to provide stringent tests and challenges for advanced nuclear models.

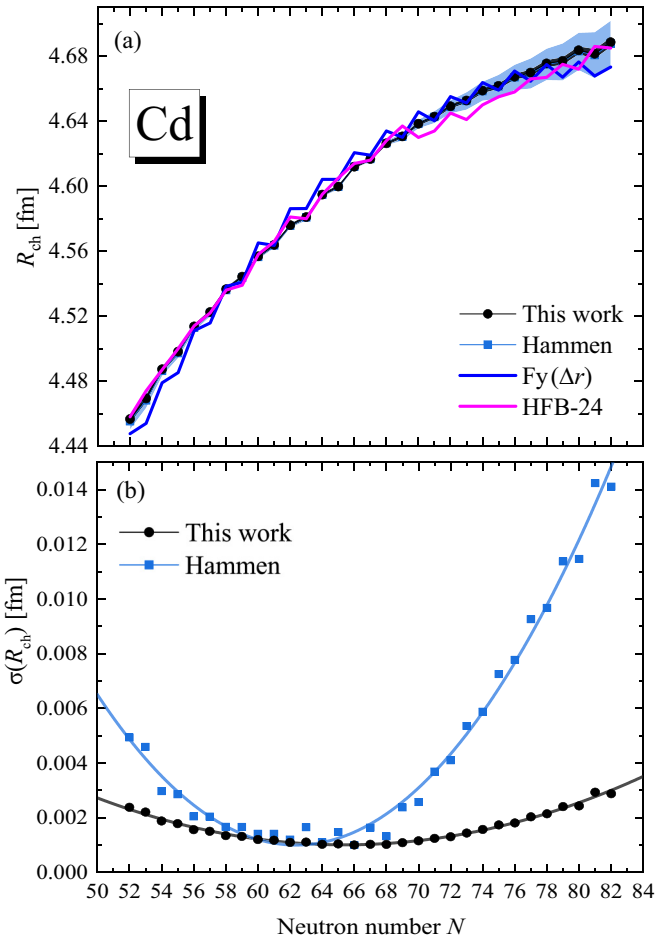

FIG. 3. (a) R_{ch} of $^{100-130}$Cd, as compared with Ref. [13] and theoretical predictions obtained using Fy(Δr) and HFB-24. The red and blue shaded regions denote the uncertainty range for this work and Ref. [13]. (b) The uncertainties $\sigma(R_{ch})$ of the R_{ch}.

VI. CONCLUSION

In this work, the $\delta\langle r^2\rangle^{A,114}$ and R_{ch} of $^{100-130}$Cd are extracted with improved precision by adopting more-accurate atomic IS factors. The IS of the 214.5-nm transition in Cd^+ is measured with higher accuracy using the ion trap and the sympathetic cooling technique. Given the new IS value, a systematic King-plot analysis is performed to determine the atomic IS factors. The accuracy of the determined factors improves nearly fourfold compared with that of previous results [13]. Furthermore, the CI+MBPT calculations are performed to cross-check the accuracy and reliability of the extracted atomic IS factors. New $\delta\langle r^2\rangle$ and R_{ch} of $^{100-130}$Cd are then extracted using the atomic IS factors given in this work. In the neutron-rich region, the accuracy of R_{ch} is improved nearly fivefold. The R_{ch} values reported in this work reveal hidden discrepancies with the previous density functional predictions [40,41,41–44] and set stringent constraints to current nuclear theories, in which newly developed density functional calculations, HFB-24 [41] and Fy(Δr) [40], fail to reproduce the present results perfectly. In addition, the accurate nuclear charge radius will be helpful in the investigation of the shell closure of Cd when expanding to the magic number of $N = 82$.

TABLE IV. Input data of the York regression. $\mu\delta\nu_{214.5}^{A,A'}$ and $\sigma(\mu\delta\nu_{214.5}^{A,A'})$ are the modified IS and its uncertainties of the Cd^+'s 214.5-nm transition, in GHz u units. $\mu\lambda_{Cd}^{A,A'}$ and $\sigma(\mu\lambda_{Cd}^{A,A'})$ are the modified nuclear size parameter and its uncertainties, in fm^2 u units.

(A, A')	$\mu\delta\nu_{214.5}^{A,A'}$	$\sigma(\mu\delta\nu_{214.5}^{A,A'})$	$\mu\lambda_{Cd}^{A,A'}$	$\sigma(\mu\lambda_{Cd}^{A,A'})$
(108,106)	−4550.7	10.7	985.7	24.0
(110,108)	−4503.4	12.0	1034.2	24.9
(112,110)	−4642.5	7.0	1041.9	25.8
(111,110)	−1393.6	40.9	531.8	51.1
(114,112)	−4289.5	5.1	986.4	26.7
(113,112)	−1492.5	32.3	563.6	53.0
(116,114)	−3433.0	9.1	853.2	27.7

ACKNOWLEDGMENTS

We thank V. A. Dzuba, W. Nörtershäuser, D. T. Yordanov, P. O. Schmidt, and F. Gulminelli for helpful discussions. This work is supported by the National Key R&D Program of China (Grants No. 2021YFA1402100, No. 2017YFE0116700, and No. 2018YFA0404400) and National Natural Science Foundation of China (Grants No. 11874064, No. 91436210, No. 12073015, No. 11935003, and No. 11875075).

APPENDIX

1. Input data of the York regression

The input data of the York regression are given in Table IV. The correlation coefficient r between $\sigma(\mu\delta\nu_{214.5}^{A,A'})$ and $\sigma(\mu\lambda_{Cd}^{A,A'})$ is 0.95.

2. Theoretical predicted R_{ch} values in Cd

The theoretical predicted R_{ch} values in $^{100-130}$Cd of the Skyrme–Hartree–Fock–Bogoliubov mass formulas HFB-24 and Fayans functioncal Fy(Δr) in Fig. 3 are given in Table V.

TABLE V. Theoretical predicted R_{ch} values in $^{100-130}$Cd of the HFB-24 and Fy(Δr) in Fig. 3. Values of the Fy(Δr) are obtained from [13].

A	N	HFB-24	Fy(Δr)
100	52	4.458	4.448
101	53	4.474	4.454
102	54	4.487	4.479
103	55	4.500	4.485
104	56	4.514	4.511
105	57	4.522	4.516
106	58	4.536	4.538
107	59	4.539	4.541
108	60	4.558	4.565
109	61	4.566	4.564
110	62	4.581	4.586
111	63	4.580	4.586
112	64	4.595	4.604

TABLE V. (*Continued.*)

A	N	HFB-24	Fy(Δr)
113	65	4.605	4.604
114	66	4.614	4.621
115	67	4.616	4.619
116	68	4.628	4.634
117	69	4.637	4.630
118	70	4.630	4.646
119	71	4.634	4.640
120	72	4.645	4.655
121	73	4.641	4.651

TABLE V. (*Continued.*)

A	N	HFB-24	Fy(Δr)
122	74	4.650	4.664
123	75	4.655	4.659
124	76	4.658	4.671
125	77	4.666	4.665
126	78	4.667	4.675
127	79	4.675	4.667
128	80	4.672	4.676
129	81	4.686	4.668
130	82	4.685	4.673

[1] Á. Koszorús, X. F. Yang, W. G. Jiang, S. J. Novario, S. W. Bai, J. Billowes, C. L. Binnersley, M. L. Bissell, T. E. Cocolios, B. S. Cooper *et al.*, Charge radii of exotic potassium isotopes challenge nuclear theory and the magic character of $N = 32$, Nat. Phys. **17**, 493 (2021).

[2] C. Gorges, L. V. Rodriguez, D. L. Balabanski, M. L. Bissell, K. Blaum, B. Cheal, R. F. GarciaRuiz, G. Georgiev, W. Gins, H. Heylen *et al.*, Laser Spectroscopy of Neutron-Rich Tin Isotopes: A Discontinuity in Charge Radii across the $N = 82$ Shell Closure, Phys. Rev. Lett. **122**, 192502 (2019).

[3] T. Day Goodacre, A. V. Afanasjev, A. E. Barzakh, B. A. Marsh, S. Sels, P. Ring, H. Nakada, A. N. Andreyev, P. VanDuppen, N. A. Althubiti *et al.*, Laser Spectroscopy of Neutron-Rich ^{207,208}Hg Isotopes: Illuminating the Kink and Odd-Even Staggering in Charge Radii across the $N = 126$ Shell Closure, Phys. Rev. Lett. **126**, 032502 (2021).

[4] B. A. Marsh, T. Day Goodacre, S. Sels, Y. Tsunoda, B. Andel, A. N. Andreyev, N. A. Althubiti, D. Atanasov, A. E. Barzakh, J. Billowes *et al.*, Characterization of the shape-staggering effect in mercury nuclei, Nat. Phys. **14**, 1163 (2018).

[5] H. De Witte, A. N. Andreyev, N. Barre, M. Bender, T. E. Cocolios, S. Dean, D. Fedorov, V. N. Fedoseyev, L. M. Fraille, S. Franchoo *et al.*, Nuclear Charge Radii of Neutron-Deficient Lead Isotopes Beyond $N = 104$ Midshell Investigated by In-Source Laser Spectroscopy, Phys. Rev. Lett. **98**, 112502 (2007).

[6] D. T. Yordanov, M. L. Bissell, K. Blaum, M. DeRydt, C. Geppert, M. Kowalska, J. Kramer, K. Kreim, A. Krieger, P. Lievens *et al.*, Nuclear Charge Radii of $^{21-32}$Mg, Phys. Rev. Lett. **108**, 042504 (2012).

[7] X. F. Yang, C. Wraith, L. Xie, C. Babcock, J. Billowes, M. L. Bissell, K. Blaum, B. Cheal, K. T. Flanagan, R. F. Garcia Ruiz *et al.*, Isomer Shift and Magnetic Moment of the Long-Lived $1/2^+$ Isomer in $^{79}_{30}$Zn$_{49}$: Signature of Shape Coexistence near ^{78}Ni, Phys. Rev. Lett. **116**, 182502 (2016).

[8] W. Geithner, T. Neff, G. Audi, K. Blaum, P. Delahaye, H. Feldmeier, S. George, C. Guenaut, F. Herfurth, A. Herlert *et al.*, Masses and Charge Radii of $^{17-22}$Ne and the Two-Proton-Halo Candidate ^{17}Ne, Phys. Rev. Lett. **101**, 252502 (2008).

[9] R. Sanchez, W. Nortershauser, G. Ewald, D. Albers, J. Behr, P. Bricault, B.A. Bushaw, A. Dax, J. Dilling, M. Dombsky *et al.*, Nuclear Charge Radii of ^{9,11}Li: The Influence of Halo Neutrons, Phys. Rev. Lett. **96**, 033002 (2006).

[10] W. Nörtershäuser, D. Tiedemann, M. Zakova, Z. Andjelkovic, K. Blaum, M.L. Bissell, R. Cazan, G.W.F. Drake, C. Geppert, M. Kowalska *et al.*, Nuclear Charge Radii of ^{7,9,10}Be and the One-Neutron Halo Nucleus ^{11}Be, Phys. Rev. Lett. **102**, 062503 (2009).

[11] G. Hagen, A. Ekström, C. Forssén, G. R. Jansen, W. Nazarewicz, T. Papenbrock, K. A. Wendt, S. Bacca, N. Barnea, B. Carlsson *et al.*, Neutron and weak-charge distributions of the ^{48}Ca nucleus, Nat. Phys. **12**, 186 (2016).

[12] F. Gebert, Y. Wan, F. Wolf, C. N. Angstmann, J. C. Berengut, and P. O. Schmidt, Precision Isotope Shift Measurements in Calcium Ions Using Quantum Logic Detection Schemes, Phys. Rev. Lett. **115**, 053003 (2015).

[13] M. Hammen, W. Nörtershäuser, D. L. Balabanski, M. L. Bissell, K. Blaum, I. Budincevic, B. Cheal, K. T. Flanagan, N. Frommgen, G. Georgiev *et al.*, From Calcium to Cadmium: Testing the Pairing Functional through Charge Radii Measurements of $^{100-130}$Cd, Phys. Rev. Lett. **121**, 102501 (2018).

[14] I. Morrison, and R. Smith, The interacting boson approximation and the spectroscopy of the even cadmium and tin isotopes, Nucl. Phys. A **350**, 89 (1980).

[15] R. Wenz, A. Timmermann, and E. Matthias, Subshell effect in mean square charge radii of stable even cadmium isotopes, Z. Phys. A: Atoms Nuclei **303**, 87 (1981).

[16] K. Miao, J. W. Zhang, X. L. Sun, S. G. Wang, A. M. Zhang, K. Liang, and L. J. Wang, High accuracy measurement of the ground-state hyperfine splitting in a ^{113}Cd$^+$ microwave clock, Opt. Lett. **40**, 4249 (2015).

[17] J. Z. Han, H. R. Qin, N. C. Xin, Y. M. Yu, V. A. Dzuba, J. W. Zhang, and L. J. Wang, Toward a high-performance transportable microwave frequency standard based on sympathetically cooled ^{113}Cd$^+$ ions, Appl. Phys. Lett. **118**, 101103 (2021).

[18] G. Fricke, and K. Heilig, *Nuclear Charge Radii* (Springer, New York, 2004).

[19] W. A. Gillespie, S. W. Brain, A. Johnston, E. W. Lees, R. P. Singhal, A. G. Slight, M. W. S. M. Brimicombe, D. N. Stacey, V. Stacey, and H. Huhnermann, Measurements of the nuclear charge distribution in the cadmium isotopes, J. Phys. G: Nucl. Phys. **1**, L6 (1975).

[20] F. Buchinger, P. Dabkiewicz, H.-J. Kluge, A. C. Mueller, and E.-W. Otten, The N-dependence of Cd mean square charge radii

($54 \leqslant N \leqslant 72$) and the nuclear moments of ^{103}Cd, Nucl. Phys. A **462**, 305 (1987).

[21] I. Angeli, and K. P. Marinova, Table of experimental nuclear ground state charge radii: An update, At. Data Nucl. Data Tables **99**, 69 (2013).

[22] Y. N. Zuo, J. Z. Han, J. W. Zhang, and L. J. Wang, Direct temperature determination of a sympathetically cooled large $^{113}Cd^+$ ion crystal for a microwave clock, Appl. Phys. Lett. **115**, 061103 (2019).

[23] R. E. March, An introduction to quadrupole ion trap mass spectrometry, J. Mass Spectrom. **32**, 351 (1997).

[24] C. J. Foot, *Atomic Physics* (Oxford University Press, New York, 2004).

[25] S. Stenholm, The semiclassical theory of laser cooling, Rev. Mod. Phys. **58**, 699 (1986).

[26] M. Herrmann, V. Batteiger, S. Knünz, G. Saathoff, Th. Udem, and T. W. Hänsch, Frequency Metrology on Single Trapped Ions in the Weak Binding Limit: The $3s_{1/2} - 3p_{3/2}$ Transition in $^{24}Mg^+$, Phys. Rev. Lett. **102**, 013006 (2009).

[27] D. J. Wineland, and W. M. Itano, Laser cooling of atoms, Phys. Rev. A **20**, 1521 (1979).

[28] M. Wang, W. J. Huang, F. G. Kondev, G. Audi, and S. Naimi, The AME 2020 atomic mass evaluation (II). Tables, graphs and references, Chin. Phys. C **45**, 030003 (2021).

[29] W. H. King, *Isotope Shifts in Atomic Spectra* (Springer Science & Business Media, New York, 2013).

[30] D. York and N. M. Evensen, Unified equations for the slope, intercept, and standard errors of the best straight line, Am. J. Phys. **72**, 367 (2004).

[31] D. C. Bishop and W. H. King, Isotope shifts in the resonance lines of Cd II and Sn IV and the size of specific mass shifts in alkali like resonance lines, J. Phys. B: At. Mol. Phys. **4**, 1798 (1971).

[32] J. Bauche, H. Hühnermann, D. N. Stacey, V. Stacey, and M. Wilson, Analysis of optical isotope shifts in cadmium, Z. Phys. A: At. Nucl. **320**, 157 (1985).

[33] J. C. Berengut, Particle-hole configuration interaction and many-body perturbation theory: Application to Hg^+, Phys. Rev. A **94**, 012502 (2016).

[34] C. Solaro, S. Meyer, K. Fisher, J. C. Berengut, E. Fuchs, and M. Drewsen, Improved Isotope-Shift-Based Bounds on Bosons beyond the Standard Model through Measurements of the $^2D_{3/2}-^{2D_{5/2}}$ Interval in Ca^+, Phys. Rev. Lett. **125**, 123003 (2020).

[35] P. Müller, K. König, P. Imgram, J. Krämer, and W. Nörtershäuser, Collinear laser spectroscopy of Ca^+: Solving the field-shift puzzle of the $4s^2S_{1/2} \rightarrow 4p^2P_{1/2,3/2}$ transitions, Phys. Rev. Research **2**, 043351 (2020).

[36] I. Counts, J. Hur, D. P. L. A. Craik, H. Jeon, C. Leung, J. C. Berengut, A. Geddes, A. Kawasaki, W. Jhe, and V. Vuletić, Evidence for Nonlinear Isotope Shift in Yb^+ Search for New Boson, Phys. Rev. Lett. **125**, 123002 (2020).

[37] W. E. Lybarger, Jr., J. C. Berengut, and J. Chiaverini, Precision measurement of the $5^2S_{1/2} - 4^2D_{5/2}$ quadrupole transition isotope shift between $^{88}Sr^+$ and $^{86}Sr^+$, Phys. Rev. A **83**, 052509 (2011).

[38] J. S. Schelfhout, and J. J. McFerran, Isotope shifts for $^1S_0 - ^3P^o_{0,1}$ Yb lines from multiconfiguration Dirac-Hartree-Fock calculations, Phys. Rev. A **104**, 022806 (2021).

[39] E. C. Seltzer, *K* x-ray isotope shifts, Phys. Rev. **188**, 1916 (1969).

[40] P.-G. Reinhard, and W. Nazarewicz, Toward a global description of nuclear charge radii: Exploring the Fayans energy density functional, Phys. Rev. C **95**, 064328 (2017).

[41] S. Goriely, N. Chamel, and J. M. Pearson, Further explorations of Skyrme-Hartree-Fock-Bogoliubov mass formulas. XIII. The 2012 atomic mass evaluation and the symmetry coefficient, Phys. Rev. C **88**, 024308 (2013).

[42] S. A. Fayans, S. V. Tolokonnikov, E. L. Trykov, and D. Zawischa, Nuclear isotope shifts within the local energy-density functional approach, Nucl. Phys. A **676**, 49 (2000).

[43] S. Goriely, Further explorations of Skyrme-Hartree-Fock-Bogoliubov mass formulas. XV: The spin-orbit coupling, Nucl. Phys. A **933**, 68 (2015).

[44] S. Goriely, N. Chamel, and J. M. Pearson, Further explorations of Skyrme-Hartree-Fock-Bogoliubov mass formulas. XVI. Inclusion of self-energy effects in pairing, Phys. Rev. C **93**, 034337 (2016).